Synoptically Driven Arctic Winter States

KIRSTIE STRAMLER
Columbia University, New York, New York

ANTHONY D. DEL GENIO
NASA Goddard Institute for Space Studies, New York, New York

WILLIAM B. ROSSOW
City College of New York, New York, New York

(Manuscript received 30 April 2010, in final form 2 November 2010)

ABSTRACT

The dense network of the Surface Heat Budget of the Arctic (SHEBA) observations is used to assess relationships between winter surface and atmospheric variables as the SHEBA site came under the influence of cyclonic and anticyclonic atmospheric circulation systems. Two distinct and preferred states of subsurface, surface, atmosphere, and clouds occur during the SHEBA winter, extending from the oceanic mixed layer through the troposphere and preceded by same-sign variations in the stratosphere. These states are apparent in distributions of surface temperature, sensible heat and longwave radiation fluxes, ocean heat conduction, cloud-base height and temperature, and in the atmospheric humidity and temperature structure.

Surface and atmosphere are in radiative–turbulent–conductive near-equilibrium during a warm opaquely cloudy-sky state, which persists up to 10 days and usually occurs during the low surface pressure phase of a baroclinic wave, although occasionally occurs during the high surface pressure phase because of low, scattered clouds. Clouds occurring in this state have near-unity emissivity and the lowest bases in the vicinity of, or below, the temperature inversion peak. A cold radiatively clear-sky state persists up to two weeks, and occurs only in the high surface pressure phase of a baroclinic wave. The radiatively clear state has clouds that are too tenuous when surface based or, irrespective of opacity, located too far aloft to contribute significantly to the surface energy budget. There is a 13-K surface temperature difference between the two states, and atmospheric inversion peak temperatures are linearly related to the surface temperature in both states. The snow–sea ice interface temperature oscillates over the course of the winter season, as it cools during the radiatively clear state and is warmed from atmospheric emission above and ocean heat conduction from below during the opaquely cloudy state.

Analysis of satellite data over the Arctic from 70°–90°N indicates that the radiatively clear and opaquely cloudy states observed at SHEBA may be representative of the entire Arctic basin. The results suggest that model formulation inadequacies should be easier to diagnose if modeled energy transfers are compared with observations using process-based metrics that acknowledge the bimodal nature of the Arctic ocean–ice–snow–atmosphere column, rather than monthly and regionally averaged quantities. Climate change projections of thinner Arctic sea ice and larger advective water vapor influxes into the Arctic could yield different frequencies of occupation of the radiatively clear and opaquely cloudy states and higher wintertime temperatures of SHEBA ocean, ice, snow, atmosphere, and clouds—in particular, a wintertime warming of the snow–sea ice interface temperature.

1. Introduction

Climate models predict polar amplification of global warming (Holland and Bitz 2003; Solomon et al. 2007), and despite significant natural variability, the anthropogenic signal appears to be emerging in observed temperatures (Serreze et al. 2009; Screen and Simmonds 2010). The rate of Arctic sea ice melt in recent decades has exceeded model predictions of polar response to the warming climate (Stroeve et al. 2007).

In the Arctic, the perennial sea ice is now considered to be in, or near, complete collapse (Lindsay and Zhang 2005; Maslanik et al. 2007b; Comiso et al. 2008). Numerous mechanisms for the accelerated sea ice decline have been

---

Corresponding author address: Kirstie Stramler, 3048 Halcyon Court #B, Berkeley, CA 94705.
E-mail: kirstie.stramler@gmail.com

DOI: 10.1175/2010JCLI3817.1

proposed, including anomalous atmospheric winds, oceanic circulation variability, preconditioning of the ice pack, black carbon deposition, solar heating of the upper ocean, downwelling longwave flux anomalies, decreased multiyear ice extent, and the Arctic dipole anomaly (DA; Rigor and Wallace 2004; Francis et al. 2005; Zhang et al. 2008; Maslanik et al. 2007b; Perovich et al. 2008; Koch et al. 2009; Wang et al. 2009; Ogi et al. 2010).

Atmospheric circulation is considered significant to recent and current Arctic ice reductions (Rigor et al. 2002; Overland and Wang 2005; Maslanik et al. 2007a) as well, and although atmospheric advection comprises the bulk of the warming that is radiated to space during Arctic winter (Nakamura and Oort 1988), we have yet to establish the mechanistic details of energy transfers into the Arctic occurring during individual storm advection events.

Walsh and Chapman (1998) found a 6°–9°C increase in Arctic surface air temperatures under overcast skies for September–March and a greater increase when observations were stratified by wind as well as by cloudiness. Changes in cloudiness, wind, and surface temperature are two important indicators of the passage of a midlatitude baroclinic disturbance (e.g., Bjerknes 1919; Lau and Crane 1995), so the Walsh and Chapman (1998) results could indicate non-monomodal winter Arctic surface temperature distributions. Non-monomodal Arctic distributions could have two climatically important implications: mean values might not be physically representative of the energy exchanges between surface and atmosphere, and an insignificant change in a mean value with climate change could mask a significant redistribution of population within the surface temperature distribution.

Were the energy exchanges that occur during storm advection events understood, climate modelers would be better able to prioritize those parameters that must be resolved to adequately represent Arctic climate. In the hopes of moving toward that goal, we use data gathered during the Surface Heat Budget of the Arctic (SHEBA) field campaign (Uttal et al. 2002) to address the following basic questions:

- How do the Arctic atmospheric temperature and moisture structure evolve when the surface, subsurface, and atmosphere are responding to a warming perturbation, and how do they respond when that perturbation is removed?
- As significant advective influxes of moisture and temperature in the Arctic occur primarily during the passage of baroclinic disturbances (e.g., Nakamura and Oort 1988; Skific et al. 2009), does the surface energy balance differ greatly at these times?

In this study, the dense network of SHEBA observations is used to depict the evolving relationships between surface and atmospheric variables as the SHEBA site comes under the influence of cyclonic and anticyclonic atmospheric circulation systems. We focus here on Arctic winter, the simplest season to understand because of the absence of solar insolation and sea ice melting. A follow-up paper will explore the transition to Arctic spring and summer. In section 2, we describe the type and temporal resolution of the varied observations. In section 3, we document two preferred atmospheric states apparent in the observations, their consistent synoptic contexts, and the distinct effect each has on surface and subsurface energy exchange. In section 4, we conclude with commentary on how our results fit into the larger body of Arctic and climate literature and make recommendations for modeling priorities.

2. Data sources and analysis methods

The highest possible time resolution common to most of the instruments detailed below was retained (essentially hourly). We rely on sampling as much as possible, rather than averaging, in an effort not to obscure any covarying properties between surface and atmosphere at time scales near the measurement resolution. Data at less than hourly resolution, for example, the rawinsonde data, were required to be taken (launched) within 20 min of the hourly surface-based observations. The cloud measurement at the end of the hour during which a given surface flux measurement was accumulated was used to determine whether clouds were present, in keeping with the persistence of SHEBA cloudy–clear skies (cloud detection in any given hour tended to be skewed toward either cloudy or clear), and with the finding that cloud amount, when clouds are present, is generally very high (Rossow and Garder 1993; Curry et al. 1996). The sign convention adopted here for the surface energy budget is that fluxes into the uppermost surface of the Arctic Ocean are positive, and fluxes out of the surface are negative.

a. Meteorological soundings

Vaisala RS80-15GH radiosondes provided temperature, pressure, relative humidity (RH), and wind twice daily from the SHEBA Ice Camp as it drifted across the Beaufort Sea from 10 October 1997 to 10 October 1998. These parameters, as well as the derived variables specific humidity and potential temperature, were averaged into 125-m or 15-mb bins, after passing the quality control procedures described in the following paragraph. Vaisala RS80-A and RS80-H sensors are known to exhibit a dry bias of 2%–10% RH under cold, dry conditions, the bias amplified as temperatures decrease below 233 K (e.g., Elliot and Gaffen 1991; Miloshevich et al. 2001; Vomel et al. 2007); however, as this study is concerned with winter temperatures in the lower 2 km at SHEBA that range from 230 to 265 K, most of the SHEBA soundings are at warm enough temperatures to avoid errors above 10%.

Soundings most often fail to obtain viable data during large-magnitude advection events at SHEBA, and many soundings are missing all data above a given level or have vertical gaps. In these cases, as much of the lower-troposphere portion of the profile is retained as possible, so only those 125-m and 15-mb averages with fewer than 5 observations in the average are discarded. For those instances when a balloon lost buoyancy and descended near the surface, only that portion of the sounding for which the balloon was ascending is used. In addition, each of the 176 soundings was subjected to visual inspection to rule out spurious data.

b. *Surface meteorology, radiation, and turbulent flux data*

Surface air temperature (T_{sfc}) and surface pressure (P_{sfc}) were measured by the Atmospheric Surface Flux Group (ASFG) near the base of their meteorological tower. ASFG investigators utilized unidirectional hemispheric Eppley Precision Infrared Radiometers (PIR) to measure broadband (3.5–50 μm) longwave fluxes. Pyranometer output was sampled every 5 s, mean values computed at 1-min intervals, and then averaged every hour, producing the ASFG's hourly longwave flux data (Persson et al. 2002). The methods of Fairall et al. (1998) were used but adjusted as described in Ji and Tsay (2000).

Persson et al. (2002) estimate the instrumental uncertainty of the surface net longwave (NetLW) radiation to be ± 4 W m^{-2}, and of each longwave component to be ± 2.5 W m^{-2}, with little bias in the sensor measuring downwelling radiation (0.2 W m^{-2}) and unknown bias in the sensor measuring upwelling radiation. NetLW was calculated by differencing the coincident hourly averages of PIR upwelling longwave radiation LWU from PIR downwelling longwave radiation LWD, as NetLW = LWD − LWU.

Surface sensible and latent heat fluxes (SH and LH, respectively) were computed by ASFG investigators from sonic anemometer measurements of wind and humidity covariances, using the methods described in Persson et al. (2002). The ASFG version 6.0 data had 70% defined SH hourly values (of 2160 possible hourly winter observations), but it had so many missing LH values that computation of the surface energy budget including LH would be limited to utilizing only 28.1% of the winter hourly values. Of the defined LH values, 96% are within ± 1 W m^{-2}, yielding a monomodal distribution of mean -0.05 W m^{-2}. The missing LH values coincided with slightly warmer surface temperatures, as the mean winter value for the 1895 (88%) defined hourly T_{sfc} observations is 2 K greater than the defined LH subset of T_{sfc} values. Since the range of SHEBA winter T_{sfc} observations is 26 K, we opt here to ignore the LH values in favor of retaining the bulk of winter surface observations. We verified that our conclusions are unchanged when computations include the defined LH subset of surface observations.

c. *Vertically pointing cloud profilers*

The National Oceanic and Atmospheric Administration (NOAA) Environmental Technology Laboratory (ETL) 35-GHz Millimeter Cloud Radar (MMCR) provides measurements of radar reflectivity and Doppler velocity at 9-s sampling at 45-m intervals (Intrieri et al. 2002; Moran et al. 1998). The NOAA ETL Depolarization and Backscatter Unattended Light Detection and Ranging (DABUL) instrument operates at 523 nm. DABUL is sensitive to the cross-sectional area of cloud particles but attenuates in clouds with particles that have a large combined cross section (this can occur in optically thick clouds composed of small particles as well as in clouds composed of large particles), whereas MMCR is sensitive to the sixth power of particle size and suffers much less attenuation. The MMCR and DABUL were used in conjunction with each other to detect SHEBA clouds, but generally DABUL was determined to be the more optimal determinant of lowest cloud base and the MMCR of highest cloud height (see section 3 of Intrieri et al. (2002) for a discussion of ETL cloud and precipitation detection methods). DABUL provides backscatter and depolarization ratios at 5-s sampling at 30-m intervals; after background, range, and overlapping corrections are applied to the data, the intensity and depolarization can be thresholded to determine cloud-base and cloud-top heights for as many layers of cloud as are detected, where for each layer the depolarization ratio yields cloud phase information (Intrieri et al. 2002).

Given the dynamic range of even the primarily nonconvective Arctic atmosphere, it required not only the complementary sensitivities of the two cloud profilers, but also an intensive manual scene identification by ETL investigators, to obtain reliable cloud boundaries and cloud particle phase estimates at SHEBA (Uttal et al. 2002; Intrieri et al. 2002). Interpolated sounding data were used as model input and along with lidar–radar cloud boundary measurements to determine cloud temperature (Shupe and Intrieri 2004). The following quantities were used in this analysis: highest cloud-top height, lowest cloud-base height, and the presence–absence and altitude of any liquid in the column. These quantities were averaged into 10-min intervals from the 60-s resolution data provided.

d. Surface–subsurface temperature profiles

Cold Regions Research and Engineering Laboratory (CRREL) investigators at SHEBA obtained time series of temperature profiles through atmosphere, snow, sea ice, and ocean up to 45 cm above the sea ice surface and down to 390 cm below the sea ice surface. The thermistors positioned in a PVC tube to yield from 5–10-cm vertical intervals, reported every hour and are accurate to 1°C.

One-dimensional Fourier conduction was used to estimate the ocean's contribution to the surface energy budget. This method is particularly reliable for the linear winter subsurface temperature gradients observed at SHEBA. Fourier conduction is expressed as

$$q = -k dT/dz, \tag{1}$$

where q (W m^{-2}) is the heat flux, k the conductivity of the medium, and dT/dz the vertical temperature gradient across the medium. The values of snow and ice conductivity were determined as in Untersteiner (1961), which for a single layer of snow is a constant value $k_{\rm snow}$ = 0.31 W m^{-1} K^{-1}, and for ice is a function of the ice temperature and salinity (average values were used here),

$$K_{\rm ice} = k_o + (\beta S/T), \tag{2}$$

where k_o = 2.034 W m^{-1} K^{-1}, β = 0.117 W m^{-1} ppt^{-1}, salinity S = 1.6, and T is temperature. Conduction through the snow is also computed using $k_{\rm snow}$ = 0.14 W m^{-1} K^{-1} as suggested in Sturm et al. (2002) and $k_{\rm snow}$ = 0.39 W m^{-1} K^{-1} as suggested in Chung et al. (2010); heat flux results are compared with those obtained using the canonical, single-layer $k_{\rm snow}$ value.

e. Satellite cloud fraction and radiative fluxes

Cloud fraction and surface longwave radiative fluxes were obtained from the International Satellite Cloud Climatology Project (ISCCP; Rossow and Schiffer 1999). We chose the ISCCP FD radiative flux profile dataset, as the utilization of a newer radiative transfer model and newer input datasets has greatly reduced uncertainty in the ISCCP FD surface longwave fluxes, from 20–25 to 10–15 W m^{-2} (Zhang et al. 2004). ISCCP FD is available globally at temporal intervals of 3 h, and at spatial intervals of 2.5°. Here, we examine ISCCP FD data from 70°–90°N, excluding land-containing gridboxes, to provide an Arctic-wide context for the SHEBA data.

The ISCCP D-series data product is known to overestimate wintertime cloud amounts in the polar regions (Curry et al. 1996) due to detection difficulties that arise from the low-temperature, and low-to-inverse thermal contrast conditions there (Rossow and Schiffer 1999); therefore, this detection issue extends to daughter-product ISCCP FD, as well. Another noted problem that plagues many long-term near-surface datasets [including the Television Infrared Observation Satellite (TIROS) Operational Vertical Sounder (TOVS)] is the underestimation of high-latitude surface temperature inversion strength, which in the case of ISCCP FD, results in interpolated surface skin temperature values that can be up to 10 K greater than surface observations for snow covered areas (Zhang et al. 2006).

The 2.5° latitude by 2.5° longitude area of the ISCCP gridboxes means that the instantaneous full-sky flux is often a combination of clear and cloudy fluxes, so we decompose full-sky flux values into overcast and clear-sky contributions and weight their contributions to NetLW histograms by the cloud area fraction for overcast NetLW values, and by 1 minus the cloud fraction for clear-sky NetLW values.

3. Results

a. Character of the atmosphere at SHEBA

The SHEBA winter mean rawinsonde temperature profile and the deviations from it in time are shown in Fig. 1. SHEBA winter atmospheric temperatures exhibit abrupt transitions from 10 K colder than to 10 K warmer than the winter mean temperature profile. Both warm and cold episodes extend throughout much of the depth of the troposphere, and are often persistent, lasting for up to 10 days in the case of the warm anomalies and for up to 2 weeks during the cold anomalies. It is worth noting that, while these temperature anomalies are departures from the winter mean and thus include the seasonal trend, individual monthly mean temperatures are only a few degrees different from each other and from the winter mean temperature. Positive and negative specific humidity anomalies (see Fig. 2.20 of Stramler 2006) also occur simultaneously with same-sign temperature anomalies over the winter sea ice at SHEBA; the atmosphere either occupies a colder–drier state or a warmer–moister state.

The Arctic winter tropopause over the SHEBA site is at about 8.5 km and is demarcated in Fig. 1 by a discontinuity in the temperature anomalies, as stratospheric temperature conditions are primarily of opposite sign to those in the troposphere for the duration of each episode. That these stratospheric warmings and coolings precede their tropospheric counterparts is consistent with the tilt of blocked baroclinic waves with height (Palmen and Newton 1969).

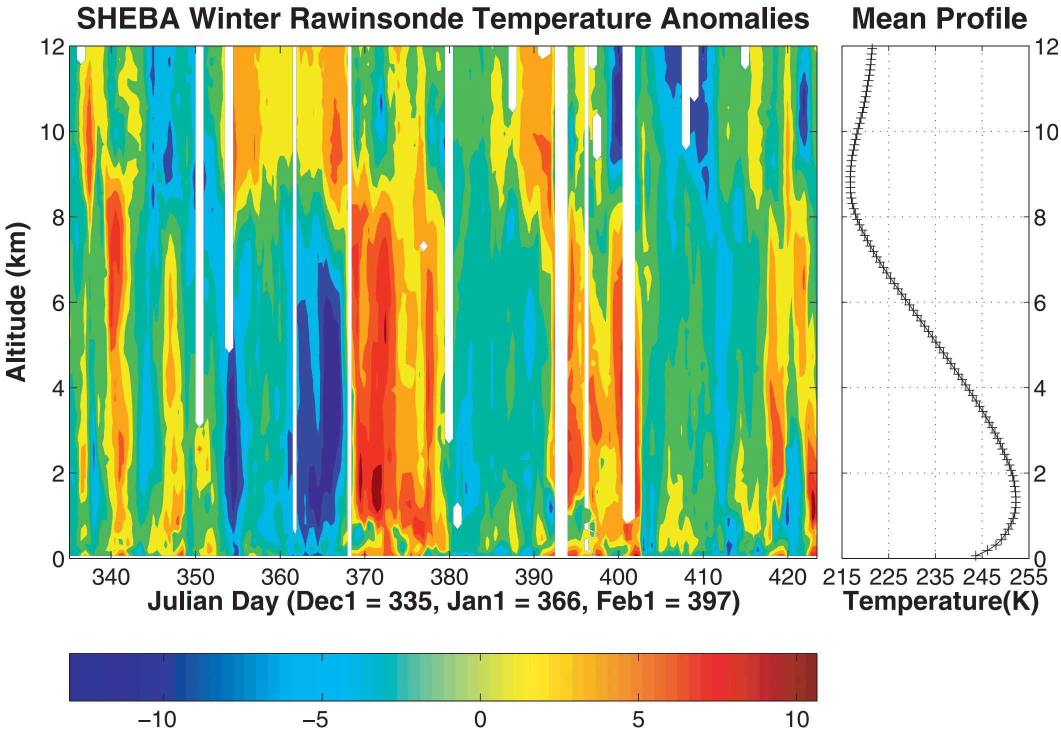

FIG. 1. Winter time series of rawinsonde temperature anomalies from 250-m vertical averages. Missing data indicated by white spaces, color bar in units Kelvin. Winter mean temperature profile from which anomalies were obtained is located to right of anomalies.

The hourly winter NetLW time series at the SHEBA surface site (upper panel, Fig. 2) ranges between −65 and 20 W m^{-2} over the course of the winter 1997/98 season. Within this range, however, NetLW preferentially occupies values near 0 and −40 W m^{-2} with higher frequency and longer persistence. These two preferred NetLW values occupy distinct modes of the SHEBA winter histogram (lower panel, Fig. 2). In general, the positive deviations from the mean temperature profile in Fig. 1 correspond to the 0 W m^{-2} NetLW occurrences and negative departures to −40 W m^{-2} NetLW occurrences. Thus, NetLW is used to sort the soundings corresponding to the warm and cold temperature anomalies of Fig. 1 into two regimes of vertical temperature and specific humidity profile histograms in Fig. 3.[1]

Atmospheric temperature and humidity structures in Fig. 3 differ markedly between the warm and cold temperature anomalies. Warm anomalies are characterized by a surface mixed layer capped by an elevated temperature inversion peaking near 2 km at roughly 255 K, surface temperatures near 250 K, and a specific humidity peak of 1.5 g kg^{-1} at 2 km.[2] Cold anomalies have no surface mixed layer and instead are characterized by a surface-based temperature inversion peaking near 1 km at roughly 250 K, surface temperatures near 237 K, and a specific humidity peak of 0.5 g kg^{-1} at 1 km. The vertical profile of relative humidity accompanying the warm anomalies exhibits RH near water saturation throughout the troposphere, whereas the cold anomaly RH vertical profiles exhibit saturated near-surface RH that quickly drops off to near 30% aloft (see Figs. 2.17 and 2.18 of Stramler 2006).

The winter SHEBA atmosphere thus exhibits two preferred states of behavior, each unique in temperature and moisture structure and preceded by same-sign stratospheric temperature anomalies. As the SHEBA atmosphere spends 87% of the winter in the preferred states (as defined using our criteria based on the bimodal NetLW histogram of Fig. 2), the winter mean temperature profile there is rarely physically realized. The existence of

---

[1] We define the primary mode, centered at −40 W m^{-2}, as all soundings for which NetLW ≤ -30 W m^{-2}, and the secondary mode, centered at 0 W m^{-2}, as those for which NetLW ≥ -10 W m^{-2}. All intermediate values are considered to be transitions between the two typical modes of winter NetLW.

[2] The surface-based mixed layers (based on potential temperature profiles not shown) beneath the elevated inversions of the warm anomaly typically range from 250–750 m in depth and are hence distorted both by histograms and by averaging, as each technique results in lapse rates of opposite signs being averaged into a single level.

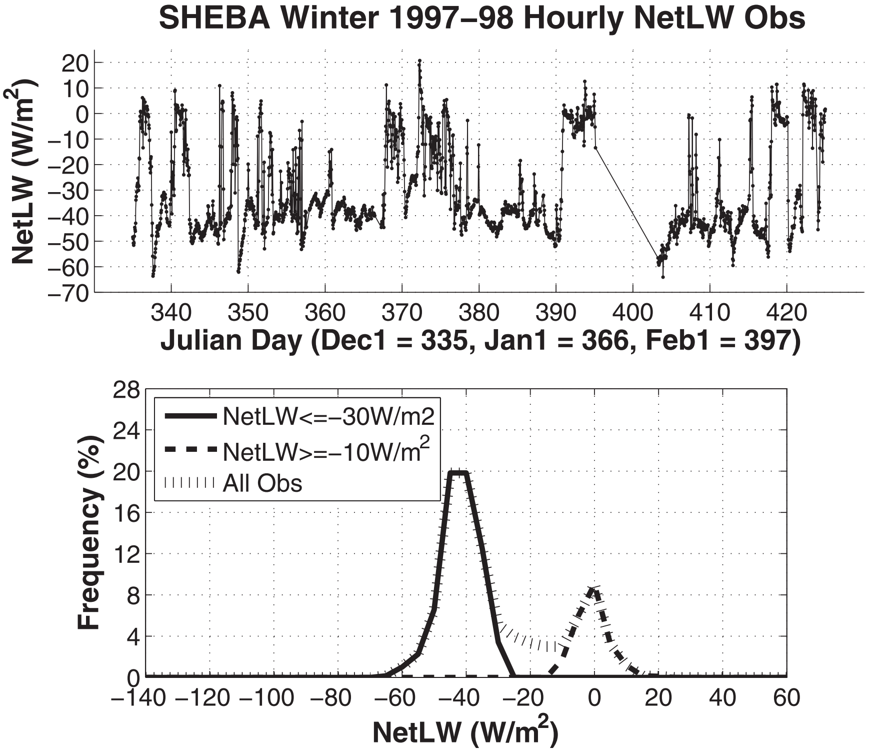

FIG. 2. (top) Interpolated time series of SHEBA winter NetLW. Each hourly observation, where available, is represented by a point. Here, the temporal distribution of missing observations is apparent, in particular the weeklong period centered near Julian day 400. (bottom) Histogram, using 5 W m^{-2} bins, of defined hourly NetLW observations (dotted) and subsets defining the modes centered at −40 (solid) and 0 W m^{-2} (dashed).

fairly discrete temperature states requires that, to represent Arctic energy transfers reasonably well, climate models will have to capture not only the temperature profiles for each state but also the frequency of occurrence of each state.

Henceforth, we refer to the two observed states as ‘‘opaquely cloudy’’ and ‘‘radiatively clear,’’ respectively. This terminology corresponds to our findings, presented in section 3c, that episodes of warm temperature anomalies usually contain near-unit emissivity clouds located at or below the peak of the elevated temperature inversion, while episodes of cold temperature anomalies contain clouds 51% of the time but with cloud emission differing little from clear-sky emission.

b. *Synoptic context of the preferred states*

While the abrupt transitions between the two preferred states occur on time scales of less than 1 h to several hours, the resulting warm and cold anomalies often persist for days to weeks (Figs. 1 and 2). We find that the persistence and abruptness are usually synoptically driven, the former from Arctic basin-scale positioning of circulation features, and the latter resulting from the rapid incursion of advective fluxes over the SHEBA site, as also seen in other seasons at SHEBA (Zuidema et al. 2005; Stramler 2006).

We have documented the correspondence of onset and duration of SHEBA winter warm and cold temperature anomalies with the passage of, respectively, the low and high surface pressure phase of baroclinic waves (see Figs. 2.25 and 2.26, and corresponding discussion, in Stramler 2006). Figure 4 illustrates the connection between the two NetLW modes and synoptic conditions: radiatively clear skies occur preferentially in combination with high surface pressure (≥1020 mb) and opaquely cloudy skies with low surface pressure.

Generally, apart from prolonged durations and occasional eastward propagation, synoptic sequences during SHEBA winter exhibit characteristics typical of a classical midlatitude baroclinic disturbance, in which a storm’s approach is heralded by decreasing surface pressure, clouds, increased surface temperatures, and increased atmospheric temperatures and humidities. To illustrate this point, Fig. 4 contains two panels of P_{sfc} plotted versus NetLW for the SHEBA winter. In the upper panel of Fig. 4, a low to the southeast (green line) and a low from

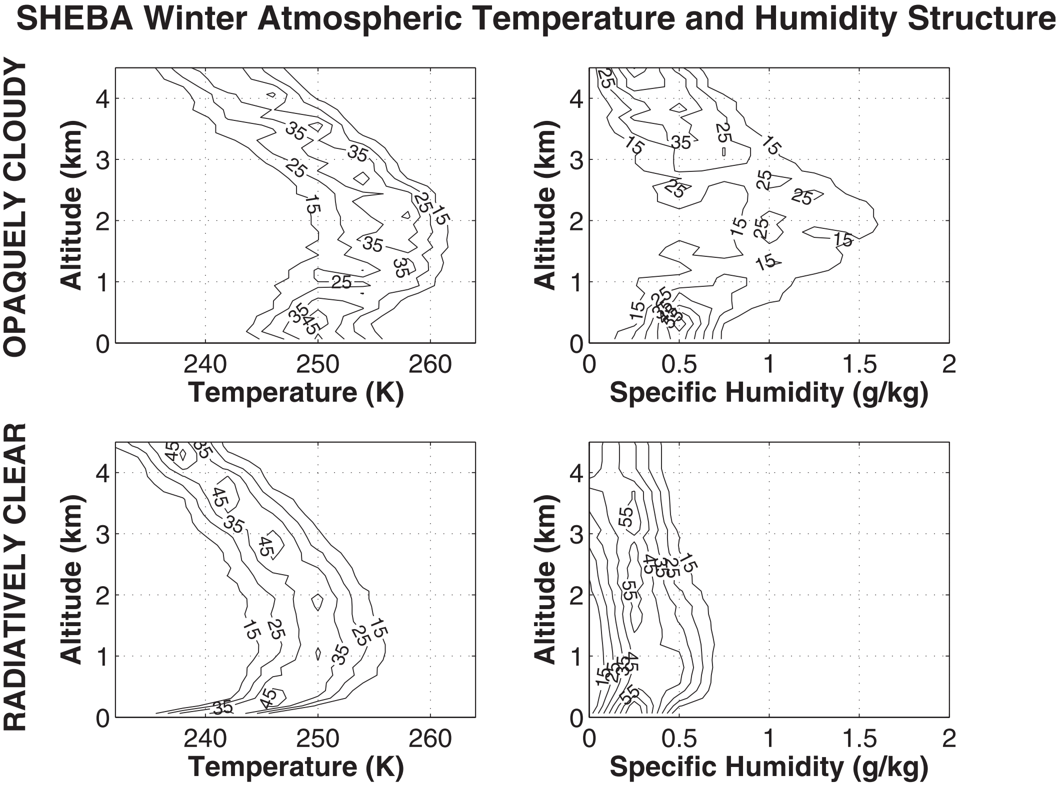

FIG. 3. (left) Vertical temperature and (right) specific humidity histograms for SHEBA winter, constructed at 125-m vertical resolution, using 4-K temperature bins, and 0.25 g kg^{-1} specific humidity bins. (top) Histograms of atmospheric structure for soundings launched while NetLW ≈ 0 W m^{-2} and (bottom) while NetLW ≈ −40 W m^{-2}. Contours describe the percent of observations at a given altitude, and are labeled in 10% increments.

the northeast (blue line) trace trajectories corresponding to the classical transitions from high P_{sfc}, low NetLW conditions to low P_{sfc}, and high NetLW conditions at the approach of a cyclonic disturbance. The low to the southeast was accompanied by the appearance of ice clouds up to heights of 5 km, and the low from the northeast by ice clouds in which the presence of liquid was detected. The red line in the upper panel of Fig. 4 is a transition in the opposite sense, where storm clouds were supplanted by clear skies, high P_{sfc}, and low NetLW.

These classical transitions do not explain the smaller number of points in Fig. 4 for which NetLW ≈ 0 W m^{-2} occurs instead with high pressure and NetLW ≈ −40 W m^{-2} with low pressure. Two events during the SHEBA winter exhibited positive P_{sfc}–NetLW correlation (red and blue trajectories in the lower panel of Fig. 4). Such cloudy high events, comprising only 24% of NetLW ≈ 0 W m^{-2} mode and 8% of $P_{\mathrm{sfc}} \geq 1020$, are an exception to the synoptically driven radiatively clear and opaquely cloudy NetLW modes. Inspection of the National Centers for Environmental Prediction (NCEP) reanalysis 2 surface pressure and 700-mb heights (figures not shown) does not indicate large changes in the synoptic situation at the time of these events, suggesting that the transitions to cloudy highs may be fairly localized occurrences of stratus or cirrus drifting over the SHEBA site. Midlatitude composites of satellite-observed cloudiness associated with baroclinic waves show that scattered cloud is often observed under high pressure after frontal passage (Lau and Crane 1995); the intermittent opaque clouds observed during the two cloudy high events at SHEBA are probably attributable to this phenomenon as well.

Hence, the SHEBA winter cold temperature anomalies of Fig. 1, with their attendant surface-based inversions and little variability about their −40 W m^{-2} NetLW values, mostly occur under the radiatively clear skies of anticyclonic circulation systems. SHEBA winter warm temperature anomalies occur primarily during the passage of cyclonic circulation systems but can occasionally occur for high P_{sfc} conditions as well.

c. Clouds and radiation in each SHEBA winter state

Longwave radiation, generally considered the largest component of the Arctic winter mean surface energy budget (e.g., Vowinckel and Orvig 1965; Chiacchio et al.

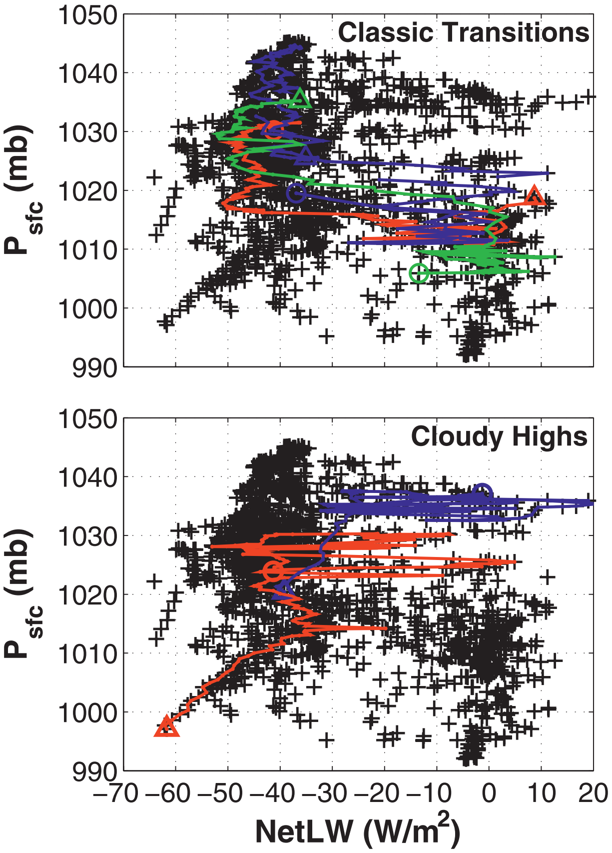

FIG. 4. SHEBA winter 1997/98 ASFG: all hourly observations of surface pressure (P_{sfc}) vs surface NetLW, indicated by black "+." (top) 3 classic transitions highlighted by tracing their NetLW–P_{sfc} evolutions: red trace corresponds to Julian day range 340.458–345; blue trace to Julian day range 362–370.375; green trace to Julian day range 388.417−395.125. Bottom: 2 cloudy high transitions: the red trace corresponds to Julian day range 348.708–353.792; blue trace to Julian day range 370.417–376. Triangle symbols correspond to initial data point of transition time series; circle symbols correspond to final data point.

2002), is the most significant determinant of the Arctic winter daily and monthly mean surface temperature field (Overland et al. 1997; Chen et al. 2003). As longwave atmospheric emission is determined by clouds and by atmospheric temperature and humidity, we first examine the nature of clouds embedded in each state, then document their influence on the surface in the following subsection.

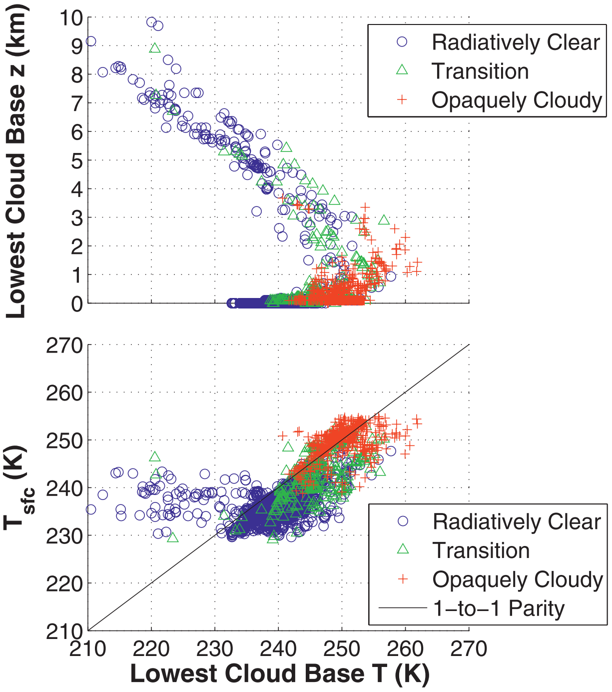

FIG. 5. (top) MMCR–lidar lowest cloud-base altitude and (bottom) ASFG surface temperature vs lowest cloud-base temperature, matched to hourly ASFG Net LW: NetLW ≥ -10 W m^{-2} indicated by red "+" symbols, those for which NetLW ≤ -30 W m^{-2} indicated by blue "○" symbols, and those for which -30 W m^{-2} < NetLW < -10 W m^{-2} by green triangles.

Over the SHEBA winter, 67% of the hourly NetLW observations corresponded to the presence of cloud. For NetLW ≈ 0 W m^{-2}, 100% of the MMCR–lidar observations indicate the presence of cloud, yet 51% of the NetLW ≈ −40 W m^{-2} observations were cloudy, as well. As noted in section 3a, there is a 13-K T_{sfc} discrepancy (250 versus 237 K) between the 0 and −40 W m^{-2} NetLW modes. When T_{sfc} observations in the −40 W m^{-2} mode are sorted into two groups—one for which a cloud is present and one for which a cloud is absent—we find that the presence of cloud is associated with a mere 2-K warmer T_{sfc}, suggesting that these are optically thin, primarily ice, clouds. Persson et al. (1999) observed that the arrival of low clouds corresponded to NetLW near 0 W m^{-2} during the Arctic night and corresponded to surface temperature increases ranging from 6°–18°C occurring over 7–84 h. This is partially consistent with the (canonically defined) winter statistics stated in the previous paragraph, and presumably the long time frame they arrived at is a consequence of sorting by cloud presence, rather than discriminating by cloud height and opacity. Categorically sorting by cloud presence and by P_{sfc} may have hampered previous Arctic studies using lower–temporal resolution data (cf. Walsh and Chapman 1998).

The altitude of the lowest cloud base (which is often but not always the altitude of maximum atmospheric emission) is plotted versus its temperature in the upper panel of Fig. 5, where observations are color coded by NetLW mode (lower panel, Fig. 2). Clouds occurring when NetLW ≈ 0 W m^{-2} have the lowest bases in the vicinity of, or below, the peak of the temperature inversion, whereas clouds occurring for NetLW ≈ −40 W m^{-2} range from being surface-based to having bases near 10 km. For NetLW ≈ -40 W m^{-2} observations, cloudy-sky LWD averages 6 W m^{-2} greater than the clear-sky LWD of 132 W m^{-2}, but this emission difference between the cloudy and clear skies is less than the respective 7 and 11 W m^{-2} LWD standard deviations of cloudy- and clear-sky LWD while NetLW ≈ -40 W m^{-2}. Furthermore, both cloudy- and clear-sky LWD for NetLW ≈ -40 W m^{-2} occupy the lower mode of the bimodal LWD distribution (not shown). For NetLW $\approx$ 0 W m^{-2}, LWD averages 220 W m^{-2}, 80–90 W m^{-2} greater than LWD for NetLW ≈ -40 W m^{-2}.

We thus infer that the clouds present for NetLW ≈ -40 W m^{-2} are either, when surface-based, too tenuous, or are, irrespective of opacity, located too far aloft to contribute significantly to the surface energy budget. We therefore refer to this state as radiatively clear and the NetLW $\approx$ 0 W m^{-2} state as opaquely cloudy.

These findings are consistent with the Shupe and Intrieri (2004) cloud forcing study, in which cloud height and temperature were shown to be the relevant parameters that determine the magnitude of the cloudy-sky longwave contribution to the Arctic surface energy budget. However, since Arctic cloud presence and properties are correlated with atmospheric temperature and humidity profiles, cloud forcing (computed by comparing clear and cloudy fluxes, as per Ramanathan et al. 1989) is an inappropriate diagnostic of cloud effects on the surface.

SHEBA cloud-base temperatures are correlated with the concurrent T_{sfc} value for both modes of the NetLW distribution (lower panel, Fig. 5), except for a few lowest cloud-base altitudes above 4–5 km that occur primarily during radiatively clear episodes. NetLW ≈ -40 W m^{-2} cloud occurrences tend to have lowest cloud bases 5–15 K warmer than the coincident T_{sfc} measurements, whereas the cloud bases observed when NetLW $\approx$ 0 W m^{-2} tend to be only a few Kelvin warmer, and sometimes colder, than the coincident T_{sfc}. Accordingly, the near-inversion peak and the near-surface clouds are the source of atmospheric emission in radiative equilibrium with the snow surface at SHEBA.

Inversion peak temperature is also linearly related to T_{sfc} (see Fig. 3.11 of Stramler 2006), offset from the 1:1 line by 10–15 K to colder T_{sfc} for radiatively clear conditions, and by 5–10 K but with more scatter under opaquely cloudy conditions. Hence, as for marine stratocumulus, SHEBA cloud vertical location is coupled in a consistent manner to the atmospheric thermodynamic structure: cloud bases in the opaquely cloudy state are located at or below the temperature inversion. For both the cloudy and the clear skies of the radiatively clear observations, the temperature inversion strength is coupled to Arctic surface temperature, consistent with HIRS satellite inferences (Liu et al. 2006).

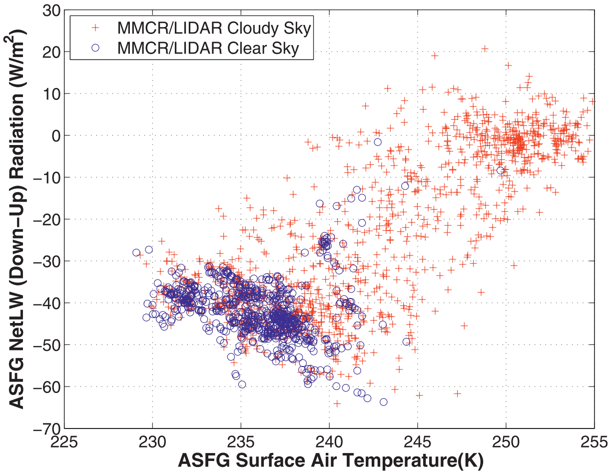

FIG. 6. All SHEBA winter 1997/98 hourly observations of ASFG NetLW vs T_{sfc}: those observations taken when MMCR–lidar yielded a cloudy decision indicated by a red "+," and a clear decision by a blue "○."

If we model the atmosphere as a graybody, then we can use the temperature at the peak of the atmospheric temperature inversion $T_{\mathrm{inv.peak}}$ to determine a value for the bulk atmospheric emissivity $\varepsilon_{\mathrm{atm}}$ for both opaquely cloudy and radiatively clear states. The scaled Stefan–Boltzmann equation in this case becomes $F = \varepsilon_{\mathrm{atm}}\sigma T^4_{\mathrm{inv.peak}}$, where F is the flux of longwave radiation emitted by the graybody in W m^{-2}, and $\sigma = 5.67 \times 10^{-8}$ W m^{-2} K^{-4} is the Stefan–Boltzmann constant. Solving for $\varepsilon_{\mathrm{atm}}$ and substituting LWD for F, we obtain $\varepsilon_{\mathrm{atm}} = \mathrm{LWD}/\sigma T^4_{\mathrm{inv.peak}}$. In the radiatively clear state, this formulation yields $\varepsilon_{\mathrm{atm}} = 0.6$, the same value Overland and Guest (1991) cite in their clear-sky modeling study, and in the opaquely cloudy state $\varepsilon_{\mathrm{atm}} = 0.9$. Given that the surface receives radiation from the colder portions of the atmosphere below the inversion, these $\varepsilon_{\mathrm{atm}}$ estimates are lower bounds for the emissivity at the layer of peak emission, so it is probable that the opaquely cloudy state clouds have near-unity emissivity.

The combined effect of varying cloud base height/temperature and varying cloud opacity causes cloudy-sky values of T_{sfc} and NetLW to encompass the entire range of possible winter values (Fig. 6). The cluster of cloudy-sky observations about NetLW $\approx$ 0 W m^{-2} is the near-unit emissivity, near-surface, and near-inversion-peak–based clouds in radiative equilibrium with the snow surface and as such exhibits zero slope. The cloudy-sky observations for NetLW ≈ -40 W m^{-2} include both the relatively transparent surface-based clouds and the higher clouds that, irrespective of emissivity, radiate at lower temperatures (upper panel, Fig. 5).

Clouds that occur for NetLW near -40 W m^{-2} exhibit the same negative NetLW–T_{sfc} trend as do the

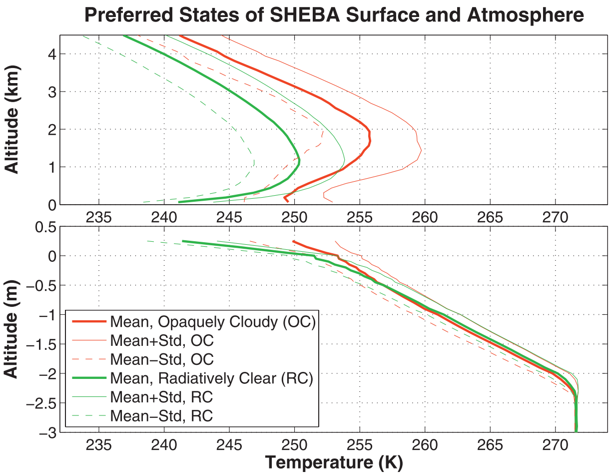

FIG. 7. (top) Mean temperatures as a function of altitude for the opaquely cloudy and radiatively clear winter states (thick red and green lines, respectively). These mean temperatures are bracketed by the mean plus one standard deviation (mean + std) and the mean minus one standard deviation (mean − std) for each mode (thin and dashed red and green lines, respectively). (bottom) As in the top panel, but for the snow, ice, and upper few centimeters of ocean. Note the ordinate axes are not to the same scale; the top panel is in km and the bottom panel in meters.

clear-sky observations. This occurs because LWU and hence T_{sfc} decreases as the surface cools less impeded to space, the T_{sfc} decrease thus gradually increasing the NetLW. This is not the case for the transitional (-10 to -30 W m^{-2}) cloudy-sky surface–atmosphere interactions, which have an overall positive NetLW–T_{sfc} trend. Under transitional NetLW cloudy skies, the positive change in NetLW results from the increasing LWD outpacing the increasing LWU as winter clouds increasingly warm the surface. The absence of solar insolation means that lesser (greater) LWD results in colder (warmer) T_{sfc}. This relation and the greater linear correlation coefficient of the hourly winter LWD with NetLW (0.94) than of LWU with NetLW (0.78) indicate that, during winter, atmospheric emission dominates the NetLW variability.

d. Surface and subsurface expression of synoptic influence

Figure 7 shows profiles of winter mean temperatures for each NetLW-diagnosed state, and their standard deviations, through the upper ocean, sea ice, snow, and atmosphere. The relative lack of variance in the warm ocean mixed layer temperature ensures that, irrespective of the influence the impinging winter atmosphere exerts on T_{sfc}, there is always a substantial temperature gradient across the ice. This is apparent from the relatively small difference in the magnitude of the temperature gradient across the sea ice between the two states, and in that their standard deviations overlap, even at the snow–sea ice interface ($\approx$0.35 m below the surface).

This temperature gradient across the snow and sea ice is linear and approximately constant during radiatively clear episodes at SHEBA, so Fourier conduction is an adequate representation of the conductive heat flux. During the radiatively clear episodes, this steep snow temperature gradient allows the escape of heat conducted through the ice, across the snow–ice interface, and through to the snow–atmosphere interface.

During opaquely cloudy episodes, however, the temperature gradient across the snow is much weaker than that across the sea ice, as T_{sfc} is coupled with the opaquely cloudy atmospheric emission, and the snow–ice interface temperature differs by only a few degrees from T_{sfc}. This impedes conductive heat transfer across the snow layer but not the sea ice for the duration of the opaquely cloudy episode. Thus, the ice–snow interface, having a small time derivative of temperature, is in near equilibrium with the ice and snow layers during the radiatively clear episodes but warms up during the opaquely cloudy episodes. It is this cumulative warming effect that may dictate the time to ice surface melt during the SHEBA spring season (Stramler 2006; K. Stramler et al. 2011, unpublished manuscript).

Hourly sea ice surface temperature fluctuations exhibit a 0.54 correlation with surface air temperature, and at 15-cm depth in the ice, the approximate T_{sfc} signal *e*-folding depth, a 0.40 correlation. This stands in contrast to the 0.96 correlation of snow surface temperature with T_{sfc}. For 5-day averages, T_{sfc} correlations with temperatures at the ice surface and at 15-cm depth improve to 0.66 and 0.50, respectively, an indication that the slower time scales of ice surface temperature variation preclude a direct correspondence between NetLW and the ocean heat transferred through the sea ice.

We can compute energy budgets for the snow layer, a reservoir having finite depth and mass, for the entire volume of snow or at either the upper (snow–atmosphere interface) or the lower (snow–sea ice interface) boundary surface. Since we are primarily concerned with snow–atmosphere interactions in this study, and as the SHEBA ASFG data proffers measured values of most components of the surface energy budget there, we choose to evaluate the energy budget at the snow–atmosphere interface.

The full surface energy budget (SEB) can be computed, neglecting horizontal energy transport, and using the upper snow surface as the reference level, using the relation

$$\mathrm{SEB} = \mathrm{NetLW} + \mathrm{NetSW} + \mathrm{LH} + \mathrm{SH} + \mathrm{OHC}, \qquad (3)$$

where OHC is the ocean heat flux conducted up through the ice and snow. Because of the dynamic variation of

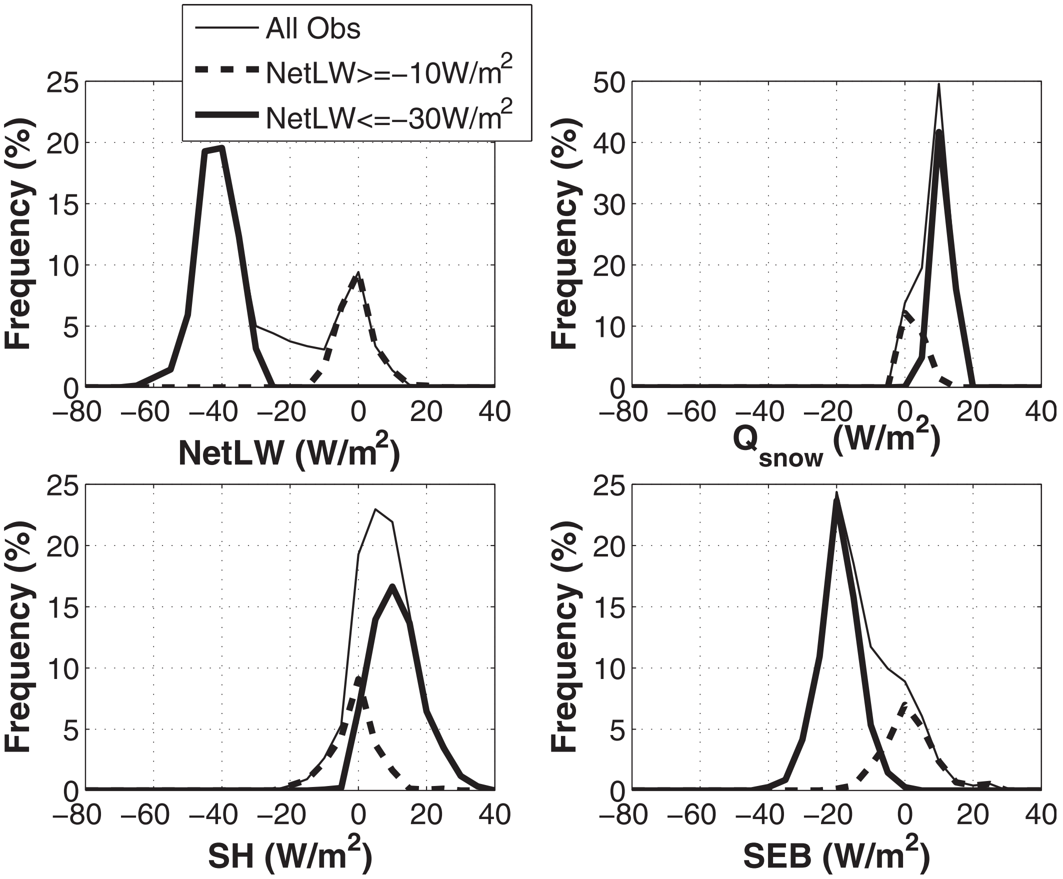

FIG. 8. Hourly observations of the significant SHEBA surface energy budget components, histogrammed for the entire winter (thin solid line), and for the two subsets of hourly observations corresponding to the opaquely cloudy and radiatively clear states (thick dashed and solid lines, respectively).

the temperature gradient across the snow, the relative invariance of heat conducted up through the ice, and because the snow surface is the reference level for the SEB, OHC can be approximated by the heat conducted across the snow layer Q_{snow}. As the winter net shortwave is zero and the winter LH is small (mean value -0.05 W m^{-2}) for both opaquely cloudy and radiatively clear episodes [perhaps due to the near-surface RH saturation with respect to ice (Andreas et al. 2002; Curry et al. 1995)], in practice this equation reduces to

$$\mathrm{SEB} = \mathrm{NetLW} + \mathrm{SH} + Q_{\mathrm{snow}}. \qquad (4)$$

As can be seen in Fig. 8, the synchronous variation of columnar temperature gradients with opaquely cloudy and radiatively clear episodes, results in bimodal histograms for each component of the SEB.

NetLW (upper-left panel) is strongly bimodal, as are LWD and LWU (not shown), because of the regularity of temperature and humidity profiles (Fig. 1) and of cloud emission, during both the opaquely cloudy and radiatively clear winter states. The surface longwave emission in both states is controlled by its temperature, which is in turn regulated by the radiative and turbulent flux from the atmosphere and by conduction from below. Overland and Guest (1991) posited a similar scenario in their modeling study of clear skies over the Arctic winter sea ice.

Sensible heat fluxes range from a 20.2 W m^{-2} cooling to a 35.9 W m^{-2} warming of the surface. When NetLW is near 0 W m^{-2} and T_{sfc} is warm, sensible heating also hovers near 0 W m^{-2} (lower-left panel, Fig. 8). When the NetLW is near -40 W m^{-2} and T_{sfc} is cold, the median sensible heating is positive, at 10.4 W m^{-2}. Thus, sensible heating warms the surface when skies are clear or have optically thin clouds and has little effect when opaque clouds are present. This difference in SH between the two NetLW modes is consistent with their different near-surface atmospheric temperature structures (Fig. 3).

Here, Q_{snow} (upper-right panel, Fig. 8) in the opaquely cloudy state has median 2.2 W m^{-2} and standard deviation 2.6 W m^{-2}, while radiatively clear state Q_{snow} has median 11.3 W m^{-2} and standard deviation 2.3 W m^{-2}.

As the temperature gradient in the snow is small in the opaquely cloudy state, the choice of k_{snow} value does not modify the median Q_{snow} appreciably. In the radiatively clear state, Q_{snow} median values and histogram peaks shift ≈50% smaller using Sturm et al. (2002) and ≈25% larger using Chung et al. (2010) k_{snow} values.

The total SEB (Fig. 8, lower right) when NetLW is near 0 W m^{-2} is itself near zero, with a median of 0.9 W m^{-2} and a standard deviation of 7.6 W m^{-2}. This arises because the individual SEB components are all near 0 W m^{-2} during those time periods. In this sense the subsurface, surface, and near-surface atmosphere at SHEBA are in a radiative, turbulent, conductive equilibrium under opaquely cloudy conditions. This stands in contrast to the −19.1 W m^{-2} median and the 6 W m^{-2} standard deviation of the SEB when NetLW is near −40 W m^{-2}. About 25% of the NetLW loss at the snow surface is compensated for by SH, and a comparable fraction compensated for by Q_{snow}; the remaining imbalance cools the surface temperature. Use of Sturm et al. (2002) k_{snow} reduces the ocean heat reaching the snow surface in the radiatively clear state, resulting in SEB ≈ −25 W m^{-2}, whereas use of Chung et al. (2010) k_{snow} augments ocean heat transfer, resulting in SEB ≈ −14 W m^{-2}.

Time series of the SEB (not shown) exhibit strong initial negative rebound spikes after episodes of near 0 W m^{-2} NetLW (near Julian days 337, 348, 377, and 420), which then equilibrate about the cooling commensurate with the large differential between the post-warm state T_{sfc}, and the much lower-atmospheric emission values. Time variation of the SEB is a consequence of time variation of temperatures within the snow layer and at the bounding surfaces of the snow layer, as it responds to conductive heat flux from the ice below and radiative losses to the atmosphere above (see Fig. 9 and discussion in section 4). Hence, the overall behavior of the ocean, sea ice, snow, atmosphere, and clouds during SHEBA winter can be characterized as acting in concert to oscillate about two synoptically driven states: one defined by the presence of near-unit emissivity clouds that induce an ice–snow interface disequilibrium and a snow–atmosphere interface near equilibrium, and the other defined by the absence of radiatively important clouds that induces an ice–snow interface near equilibrium and a snow–atmosphere interface disequilibrium.

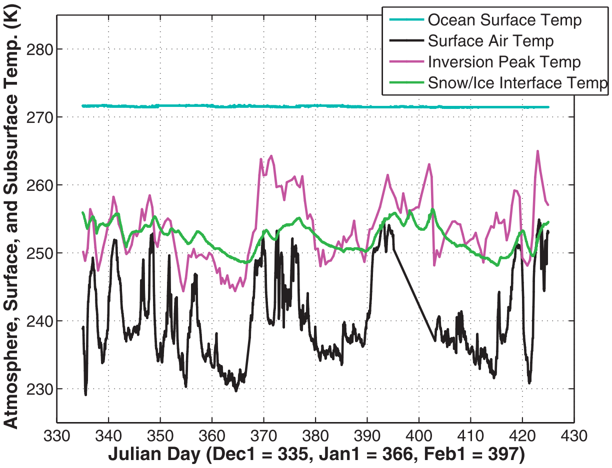

FIG. 9. SHEBA winter hourly atmosphere, surface, and subsurface temperature time series. Atmospheric inversion temperature shown for rawinsondes launched within 20 min of a surface observation.

4. Discussion

Our analysis indicates that two distinct, preferred states of subsurface, surface, atmosphere, and clouds occur during the SHEBA winter, extending from the oceanic mixed layer through much of the troposphere and preceded by same-sign variations in the stratosphere. These states are apparent in distributions of surface temperature, sensible heat and longwave radiation fluxes, ocean heat conduction, cloud-base height and temperature, and in the atmospheric humidity and temperature structure. Each state is most easily diagnosed by the corresponding value of surface NetLW since it is the component of the SEB in which the two states' distributions overlap least. The SEB indicates radiative–turbulent–conductive equilibrium during the opaquely cloudy-sky state (NetLW ≈ 0 W m^{-2}), which persists up to 10 days and typically occurs in the low surface pressure phase of a baroclinic wave, although occasionally occurs (8% of cases) for $P_{\mathrm{sfc}} \geq 1020$ mb. The radiatively clear-sky state (NetLW ≈ −40 W m^{-2}) is not in balance (SEB ≈ −19 W m^{-2}), persists up to 2 weeks, and occurs primarily in the high surface pressure phase of a baroclinic wave.

These two states can be observed in the time series of temperature at hinge points of the vertical column, as displayed in Fig. 9. The SHEBA ice–snow interface (green line) warms by several Kelvin during the prolonged opaquely cloudy episodes and then slowly cools during the even more persistent clear-sky episodes, the net effect being a trendless winter ice–snow interface temperature that oscillates only a few Kelvin about its mean. These variations are prompted by advection episodes that bring warmer atmospheric inversion peak temperatures (magenta line) and radiatively important clouds located at altitudes near and below the inversion peak. Thus, over the course of the winter, there is little loss of energy by the ocean as Arctic energy losses occur primarily through radiative cooling of the relatively warm and moist advected air masses.

Given the frequency of occurrence of these two very different preferred states (66% radiatively clear, 21%

opaquely cloudy), Arctic surface and subsurface temperatures and the winter SEB can be expected to be sensitive to changes in the frequency of opaquely cloudy-sky occurrence. It follows that increased (decreased) passage of synoptic storms during the winter season would warm (cool) the ice–snow interface to a greater (lesser) extent than observed over the SHEBA winter. The fairly sinusoidal oscillation of the ice–snow interface temperature during SHEBA winter is supplanted by a sinusoidal oscillation plus a warming trend during the SHEBA spring season, and the resulting cumulative warming may dictate the time to onset of ice surface melt during the SHEBA spring season (Stramler 2006; K. Stramler et al. 2011, unpublished manuscript).

The most plausible mechanisms thus far proposed for the recent, recurring, extreme seasonal minima of Arctic sea ice are as follows: 1) the large-scale Arctic DA, the positive phase of which exhibits sea level pressure anomalies associated with anomalous meridional winds, ice export out the Fram Strait, and augmented oceanic heat flux into the Arctic Ocean by way of the Bering Strait (Wang et al. 2009); and 2) the consequent Beaufort Gyre recirculation of the perennial sea ice (Rigor and Wallace 2004), resulting in a diminished volume of older, thicker sea ice in the Arctic Ocean. The DA alone accounts for all but one of the recent extreme minima in Arctic sea ice (Wang et al. 2009) and is consistent with previous studies, such as the increased flushing of ice out of the Fram Strait (e.g., Rigor and Wallace 2004) and numerical experiments performed by Makshtas et al. (2003) that indicate that the sea ice thickness decrease occurs primarily through a decrease in the concentration of ridged ice.

Our study suggests that the resulting distribution of younger, less-ridged sea ice is warmed by the increase in the persistent cloud and lower-atmospheric emission and the ocean heat conduction occurring during the opaquely cloudy state. Because ice temperatures are thereby maintained, the sea ice does not thicken in wintertime via bottom accretion. This is consistent with the observed net decrease in SHEBA ice thickness over an annual cycle (Perovich and Elder 2001) and with the positive ice–temperature feedback that the recent studies by Serreze et al. (2009) and Screen and Simmonds (2010) indicate is currently operating.

The large energetic difference between the two winter near-equilibrium states at SHEBA, coupled with the low frequency of occupation of intermediate states, serves as an admonition against averaging, for the average values of quantities such as NetLW (-30.2 W m^{-2}) and T_{sfc} (240.2 K) are rarely realized in nature. In addition, averaged quantities can mask a climatically important shift, as they may change only slightly in response to a systematic redistribution in frequency of occupation and modal values of radiatively clear and opaquely cloudy states.

The extent to which SHEBA is representative of the Arctic as a whole cannot be determined directly but indirect inferences can be made using satellite-derived cloud and radiative flux retrievals. A cloud-weighted NetLW histogram constructed by following the trajectory of the SHEBA field experiment through ISCCP FD grid space for January 1998 (upper panel, Fig. 10) indicates that the satellite-inferred NetLW distribution compares well to the SHEBA NetLW distribution (lower panel, Fig. 2) in that it is bimodal and has peaks near those exhibited by the in situ SHEBA observations. The most striking difference between the two NetLW distributions is the reversal of the relative populations of the radiatively clear and opaquely cloudy-sky NetLW modes in the ISCCP FD data, as compared with the SHEBA data. This is likely due to the ISCCP overestimation of wintertime cloudy-sky occurrences mentioned earlier. Another difference of note is that the ISCCP FD radiatively clear-sky mode is centered at NetLW ≈ -60 W m^{-2}, 20 W m^{-2} lower than observed at the SHEBA site; this is likely attributable to the larger ISCCP FD surface skin temperatures mentioned earlier. The opaquely cloudy-sky NetLW mode of the ISCCP FD NetLW histogram is shifted 10 W m^{-2} higher than the corresponding NetLW mode at SHEBA because the TOVS atmospheric profiles used in the retrievals exhibit no inversion and thus yield below-cloud temperatures that are too warm, increasing LWD and hence NetLW under overcast skies.

A cloud-weighted NetLW histogram constructed for the entire Arctic for January 1998, using ISCCP FD NetLW values from 70°–90°N and excluding land-containing grids (lower panel, Fig. 10), is also bimodal, indicating that the radiatively clear and opaquely cloudy winter NetLW modes observed at SHEBA are applicable to other parts of the Arctic as well. The larger sample size of the Arctic-wide ISCCP FD NetLW histogram relative to the SHEBA-tracked ISCCP FD histogram (upper panel, Fig. 10), seems to have diminished the extent of the known bias toward opaquely cloudy skies in the ISCCP FD data. There is greater variability in the NetLW values comprising the two modes over the Arctic basin, which is to be expected since temperature, humidity, etc., vary geographically over the Arctic. Regardless, the bimodal character of the Arctic-wide NetLW histogram indicates that the radiatively clear and opaquely cloudy states observed at SHEBA may indeed have analogs that span the Arctic basin and suggests caution in interpreting winter mean polar cap energy budget components (e.g., Oort 1974; Nakamura and Oort 1988), which combine the effects of both states as if they occurred simultaneously.

Similarly, it is difficult to assess the performance of models from validation studies that compare monthly averages of Arctic surface energy budget components

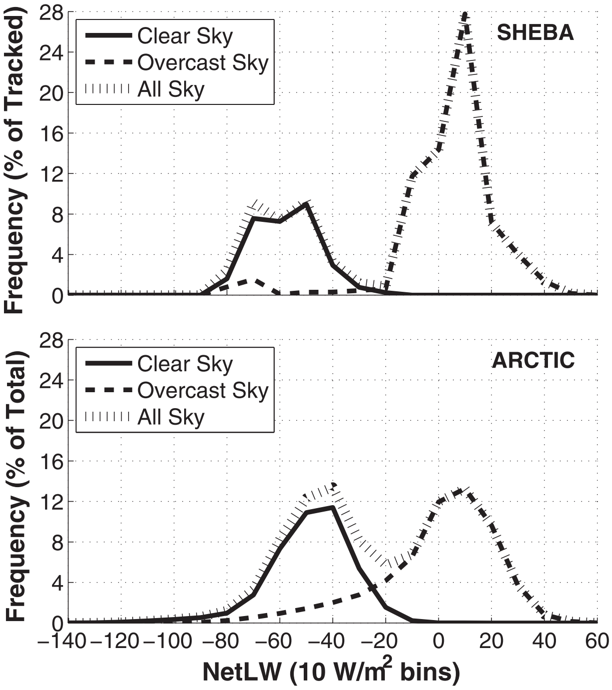

FIG. 10. Cloud-weighted histograms of ISCCP FD NetLW observations for January 1998 (see section 2e for histogram construction method). (top) 3-hourly ISCCP FD NetLW observations at location of the SHEBA ship. (bottom) 3-hourly ISCCP FD NetLW observations for Arctic region, 70–90°N, excluding land-containing grid boxes.

(e.g., Sorteberg et al. 2007, their Fig. 2) as the models may obtain a representative monthly average LWD, LWU, or NetLW value by making compensating errors in the frequency of occurrence of, and the physical values of, radiatively clear and opaquely cloudy state atmospheric structure and opacity. It is unclear whether such a representative monthly average value in say, NetLW, would correspond to representative monthly averages of SH and Q_{snow}. Arctic-wide and zonal averaging present analogous difficulties since the regional surface energy budget components may depend on the meridionally varying magnitude and frequency of atmospheric heat and moisture influxes (Sorteberg and Walsh 2008) and upon local snow and ice thicknesses. These may be factors that broaden the Arctic radiatively clear and opaquely cloudy-sky ISCCP FD NetLW modes (lower panel, Fig. 10) with respect to those observed at SHEBA.

It should be easier to diagnose model formulation inadequacies if modeled energy transfers are compared with observations using process-based metrics that acknowledge the bimodal nature of the Arctic ocean–ice–snow–atmosphere column. For example, if model output and observations were sorted by hourly or daily values of NetLW, it could be determined whether models that do not statistically or physically allow a temperature gradient in the snow layer—one that can respond to the varying atmospheric state—are capable of reproducing the energy transfers observed at SHEBA.

Arctic weather events and climate regimes take place within the confines of the circumpolar atmospheric circulation and are therefore subject to different large-scale constraints than are their midlatitude counterparts. By virtue of being upstream of the Rocky Mountains, the Western Arctic site of the SHEBA field campaign upon the Beaufort Sea Gyre pack ice is subject to transient and stationary eddies generated by topographic interactions with the primary midlatitude jet (Overland et al. 1997). Blocking in this region is responsible for the persistence of both the cyclonic and anticyclonic SHEBA winter synoptic-scale circulations observed in this study.

The resulting persistent warm and cold temperature anomalies have been shown here to have a remarkably consistent atmospheric temperature and humidity structure. The reason for this structural regularity of different wintertime circulation systems is not obvious, although it may be related to consistent source regions for the synoptic systems, to surface conditioning of air masses as they travel over the sea ice to the SHEBA site, and to radiative cooling that air masses undergo as they travel poleward. This regularity is not observed during the SHEBA spring season (Stramler 2006). Despite the indication in the ISCCP FD data that the NetLW modes may be an Arctic-wide phenomenon, because NetLW is the difference between atmospheric and surface emission, different emission magnitudes from the two entities can yield the same NetLW values. Hence, the distinctive regularity of the SHEBA winter air masses may not extend to the remainder of the Arctic basin; rather, given the accessibility to, and variability of, air masses entering the Arctic by way of the North Atlantic storm track, the Eastern Arctic winter season may be more likely to resemble the SHEBA spring season.

The NetLW distribution observed during spring and summer at SHEBA exhibits both similarities to and differences with that documented here for the winter season. The opaquely cloudy mode is present in all seasons and becomes more dominant in spring and summer, which are more overcast than winter, while a broad range of negative NetLW values in spring and summer replaces the distinct radiatively clear mode we see in winter (Stramler 2006). The winter states do have relevance to the spring season at SHEBA in that the observable persistence of distinct radiatively clear and opaquely cloudy states (albeit of differing temperatures and humidities, unlike the winter season) into SHEBA spring seems to be involved in the timing of sea ice melt. This will be discussed in a future paper (K. Stramler et al. 2011, unpublished manuscript).

If climate change predictions of a further decreasing perennial icepack (e.g., Maslanik et al. 2007b), an intensified storm track north of the British Isles (e.g., Bengtsson et al. 2006), and increased extratropical water vapor transport northward (e.g., Skific et al. 2009) are correct, then the future conditions during the winter season over the Beaufort Sea may not resemble those observed during the SHEBA winter. Thinner sea ice and larger advective influxes of water vapor could yield different frequencies of occupation of the radiatively clear and opaquely cloudy states, as well as higher temperatures at the interfaces between atmosphere, snow, and ice. It is also possible that a minimum threshold of ice thickness and/or a maximum threshold of atmospheric temperature/moisture may exist, below/above which the SHEBA column constituents will not couple in the manner described here in a future winter Arctic climate.

Acknowledgments. This research was supported by the DOE Atmospheric System Research Program and the NASA Modeling and Analysis Program (MAP). William B. Rossow was supported by NASA MAP Grant NNXD7AN04G. We thank the SHEBA ASFG members Ed Andreas, Chris Fairall, Peter Guest, and Ola Persson for the surface temperature and flux data, Taneil Uttal, Matthew Shupe, and Janet Intrieri for the ETL cloud data, Richard Moritz for the rawinsonde data, and Don Perovich for the subsurface temperature data. We also thank Yuanchong Zhang for his guidance on acquiring, reading, and land masking the ISCCP data. Three reviewers provided constructive comments that improved the paper.

REFERENCES

Andreas, E. L, P. S. Guest, P. O. G. Persson, C. W. Fairall, T. W. Horst, R. E. Moritz, and S. R. Semmer, 2002: Near-surface water vapor over polar sea ice is always near ice saturation. *J. Geophys. Res.,* **107,** 8033, doi:10.1029/2000JC000411.

Bengtsson, L., K. Hodges, and E. Roeckner, 2006: Storm tracks and climate change. *J. Climate,* **19,** 3518–3543.

Bjerknes, J., 1919: On the structure of moving cyclones. *Mon. Wea. Rev.,* **47,** 95–99.

Chen, Y., J. R. Miller, J. A. Francis, G. L. Russell, and F. Aires, 2003: Observed and modeled relationships among Arctic climate variables. *J. Geophys. Res.,* **108,** 4799, doi:10.1029/2003JD003824.

Chiacchio, M., J. Francis, and P. Stackhouse Jr., 2002: Evaluation of methods to estimate the surface downwelling longwave flux during Arctic winter. *J. Appl. Meteor.,* **41,** 306–318.

Chung, Y.-C., S. Belair, and J. Mailhot, 2010: Simulation of snow on arctic sea ice using a coupled snow–ice model. *J. Hydrometeor.,* **11,** 199–210.

Comiso, J., C. Parkinson, R. Gersten, and L. Stock, 2008: Accelerated decline in the Arctic sea ice cover. *Geophys. Res. Lett.,* **35,** L01703, doi:10.1029/2007GL031972.

Curry, J. A., J. L. Schramm, M. Serreze, and E. E. Ebert, 1995: Water vapor feedback over the Arctic Ocean. *J. Geophys. Res.,* **100,** 14 223–14 230.

——, W. B. Rossow, D. Randall, and J. L. Schramm, 1996: Overview of Arctic cloud and radiation characteristics. *J. Climate,* **9,** 1731–1764.

Elliot, W., and D. Gaffen, 1991: On the utility of radiosonde humidity archives for climate studies. *Bull. Amer. Meteor. Soc.,* **72,** 1507–1520.

Fairall, C., P. Persson, E. Bradley, R. Payne, and S. Anderson, 1998: A new look at calibration and use of Eppley Precision Infrared Radiometers. Part I: Theory and application. *J. Atmos. Oceanic Technol.,* **15,** 1229–1242.

Francis, J., E. Hunter, J. Key, and X. Wang, 2005: Clues to variability in Arctic minimum sea ice extent. *Geophys. Res. Lett.,* **32,** L21501, doi:10.1029/2005GL024376.

Holland, M., and C. Bitz, 2003: Polar amplification of climate change in coupled models. *Climate Dyn.,* **21,** 221–232.

Intrieri, J., M. Shupe, T. Uttal, and B. McCarty, 2002: An annual cycle of Arctic cloud characteristics observed by radar and lidar at SHEBA. *J. Geophys. Res.,* **107,** 8030, doi:10.1029/2000JC000423.

Ji, Q., and S.-C. Tsay, 2000: On the dome effect of Eppley Pyrgeometers and Pyranometers. *Geophys. Res. Lett.,* **27,** 971–974.

Koch, D., S. Menon, A. Del Genio, R. Ruedy, I. Aleinov, and G. Schmidt, 2009: Distinguishing aerosol impacts on climate over the past century. *J. Climate,* **22,** 2659–2677.

Lau, N.-C., and M. Crane, 1995: A satellite view of the synoptic-scale organization of cloud properties in mid-latitude and tropical circulation systems. *Mon. Wea. Rev.,* **123,** 1984–2006.

Lindsay, R., and J. Zhang, 2005: The thinning of Arctic sea ice, 1988–2003: Have we passed a tipping point? *J. Climate,* **18,** 4879–4894.

Liu, Y., J. Key, A. Schweiger, and J. Francis, 2006: Characteristics of satellite-derived clear-sky atmospheric temperature inversion strength in the Arctic, 1980–96. *J. Climate,* **19,** 4902–4913.

Makshtas, A., S. Shoutilin, and E. Andreas, 2003: Possible dynamic and thermal causes for the recent decrease in sea ice in the Arctic Basin. *J. Geophys. Res.,* **108,** 3232, doi:10.1029/2001JC000878.

Maslanik, J., S. Drobot, C. Fowler, W. Emery, and R. Barry, 2007a: On the Arctic climate paradox and the continuing role of atmospheric circulation in affecting sea ice conditions. *Geophys. Res. Lett.,* **34,** L03711, doi:10.1029/2006GL028269.

——, C. Fowler, J. Stroeve, S. Drobot, J. Zwally, D. Yi, and W. Emery, 2007b: A younger, thinner Arctic ice cover: Increased potential for rapid, extensive sea-ice loss. *Geophys. Res. Lett.,* **34,** L24501, doi:10.1029/2007GL032043.

Miloshevich, L., H. Vomel, A. Paukkunen, A. Heymsfield, and S. Oltmans, 2001: Characterization and correction of relative humidity measurements from Vaisala RS80-A radiosondes at cold temperatures. *J. Atmos. Oceanic Technol.,* **18,** 135–156.

Moran, K., B. Martner, M. Post, R. Kropfli, D. Welsh, and K. Widener, 1998: An unattended cloud-profiling radar for use in climate research. *Bull. Amer. Meteor. Soc.,* **79,** 443–455.

Nakamura, N., and A. H. Oort, 1988: Atmospheric heat budgets of the polar regions. *J. Geophys. Res.,* **93,** 9510–9524.

Ogi, M., K. Yamazaki, and J. Wallace, 2010: Influence of winter and summer surface wind anomalies on summer Arctic sea ice extent. *Geophys. Res. Lett.,* **37,** L07701, doi:10.1029/2009GL042356.

Oort, A. H., 1974: Year-to-year variations in the energy balance of the Arctic atmosphere. *J. Geophys. Res.,* **79,** 1253–1260.

Overland, J. E., and P. S. Guest, 1991: The Arctic snow and air temperature budget over sea ice during winter. *J. Geophys. Res.,* **96,** 4651–4662.

——, and M. Wang, 2005: The Arctic climate paradox: The recent decrease of the Arctic Oscillation. *Geophys. Res. Lett.,* **32,** L06701, doi:10.1029/2004GL021752.

——, J. Adams, and N. Bond, 1997: Regional variation of winter temperatures in the Arctic. *J. Climate,* **10,** 821–837.

Palmen, E., and C. Newton, 1969: *Atmospheric Circulation Systems*. International Geophysics Series, Vol. 13, Academic Press, 603 pp.

Perovich, D., and B. Elder, 2001: Temporal evolution of Arctic sea ice temperature. *Ann. Glaciol.,* **33,** 207–211.

——, J. Richter-Menge, K. Jones, and B. Light, 2008: Sunlight, water, and ice: Extreme Arctic sea ice melt during summer of 2007. *Geophys. Res. Lett.,* **35,** L11501, doi:10.1029/2008GL034007.

Persson, P. O. G., T. Uttal, J. Intrieri, C. W. Fairall, E. Andreas, and P. Guest, 1999: Observations of large thermal transitions during the Arctic night from a suite of sensors at SHEBA. Preprints, *Fifth Conf. on Polar Meteorology and Oceanography,* Dallas, TX, Amer. Meteor. Soc., 306–309.

——, C. W. Fairall, E. L Andreas, P. S. Guest, and D. K. Perovich, 2002: Measurements near the atmospheric surface flux group tower at SHEBA: Near-surface conditions and surface energy budget. *J. Geophys. Res.,* **107,** 8045, doi:10.1029/2000JC000705.

Ramanathan, V., R. Cess, E. F. Harrison, P. Minnis, B. Barkstrom, E. Ahmad, and D. Hartmann, 1989: Cloud-radiative forcing and climate: Results from the earth radiation budget experiment. *Science,* **243,** 138–140.

Rigor, I., and J. Wallace, 2004: Variations in the age of Arctic sea-ice and summer sea-ice extent. *Geophys. Res. Lett.,* **31,** L09401, doi:10.1029/2004GL019492.

——, ——, and R. Colony, 2002: Response of sea ice to the Arctic Oscillation. *J. Climate,* **15,** 2648–2663.

Rossow, W., and L. Garder, 1993: Cloud detection using satellite measurements of infrared and visible radiances for ISCCP. *J. Climate,* **6,** 2341–2369.

——, and R. Schiffer, 1999: Advances in understanding clouds from ISCCP. *Bull. Amer. Meteor. Soc.,* **80,** 2261–2287.

Screen, J., and I. Simmonds, 2010: The central role of diminishing sea ice in recent Arctic temperature amplification. *Nature,* **464,** 1334–1337.

Serreze, M., A. Barrett, D. Kindig, and M. Holland, 2009: The emergence of surface-based Arctic amplification. *Cryosphere,* **3,** 11–19.

Shupe, M., and J. Intrieri, 2004: Cloud radiative forcing of the Arctic surface: The influence of cloud properties, surface albedo, and solar zenith angle. *J. Climate,* **17,** 616–628.

Skific, N., J. Francis, and J. Cassano, 2009: Attribution of projected changes in atmospheric moisture transport in the Arctic: A self-organizing map perspective. *J. Climate,* **22,** 4135–4153.

Solomon, S., D. Qin, M. Manning, M. Marquis, K. Averyt, M. M. B. Tignor, H. L. Miller Jr., and Z. Chen, Eds., 2007: *Climate Change 2007: The Physical Science Basis*. Cambridge University Press, 996 pp.

Sorteberg, A., and J. Walsh, 2008: Seasonal cyclone variability at 70°N and its impact on moisture transport into the Arctic. *Tellus,* **60A,** 570–586.

——, V. Kattsov, J. Walsh, and T. Pavlova, 2007: The Arctic surface energy budget as simulated with the IPCC AR4 AOGCMs. *Climate Dyn.,* **29,** 131–156.

Stramler, K., 2006: The influence of synoptic atmospheric motions on the Arctic energy budget. Ph.D. thesis, Columbia University, 269 pp.

Stroeve, J., M. Holland, W. Meier, T. Scambos, and M. Serreze, 2007: Arctic sea ice decline: Faster than forecast. *Geophys. Res. Lett.,* **34,** L09501, doi:10.1029/2007GL029703.

Sturm, M., D. Perovich, and J. Holmgren, 2002: Thermal conductivity and heat transfer through the snow on the ice of the Beaufort Sea. *J. Geophys. Res.,* **107,** 8043, doi:10.1029/2000JC000409.

Untersteiner, N., 1961: On the mass and heat budget of Arctic sea ice. *Meteor. Atmos. Phys.,* **A12,** 151–182.

Uttal, T., and Coauthors, 2002: Surface heat budget of the Arctic Ocean. *Bull. Amer. Meteor. Soc.,* **83,** 255–275.

Vomel, H., and Coauthors, 2007: Radiation dry bias of the Vaisala RS92 humidity sensor. *J. Atmos. Oceanic Technol.,* **24,** 953–963.

Vowinckel, E., and S. Orvig, 1965: Energy balance of the Arctic, V. *Theor. Appl. Climatol.,* **14,** 303–325.

Walsh, J. E., and W. L. Chapman, 1998: Arctic cloud-radiation-temperature associations in observational data and atmospheric reanalyses. *J. Climate,* **11,** 3030–3045.

Wang, J., J. Zhang, E. Watanabe, M. Ikeda, K. Mizobata, J. Walsh, X. Bai, and B. Wu, 2009: Is the dipole anomaly a major driver to record lows in Arctic summer sea ice extent? *Geophys. Res. Lett.,* **36,** L05706, doi:10.1029/2008GL036706.

Zhang, J., R. Lindsay, M. Steele, and A. Schweiger, 2008: What drove the dramatic retreat of Arctic sea ice during summer 2007? *Geophys. Res. Lett.,* **35,** L11505, doi:10.1029/2008GL034005.

Zhang, Y., W. Rossow, A. Lacis, V. Oinas, and M. Mishchenko, 2004: Calculation of radiative fluxes from the surface to top of atmosphere based on ISCCP and other global data sets: Refinements of the radiative transfer model and the input data. *J. Geophys. Res.,* **109,** D19105, doi:10.1029/2003JD004457.

——, ——, and P. Stackhouse Jr., 2006: Comparison of different global information sources used in surface radiative flux calculation: Radiative properties of the near-surface atmosphere. *J. Geophys. Res.,* **111,** D13106, doi:10.1029/2005JD006873.

Zuidema, P., and Coauthors, 2005: An Arctic springtime mixed-phase cloudy boundary layer observed during SHEBA. *J. Atmos. Sci.,* **62,** 160–176.